Preprints of the 21st IFAC World Congress (Virtual)
Berlin, Germany, July 12-17, 2020

Development and stabilization of a low-cost single-tilt tricopter ⋆

Daniel Abara [*,**] **Somasundar Kannan** [*] **Alexander Lanzon** [*]

[*] *Control Systems Centre, Department of Electrical and Electronic Engineering, School of Engineering, University of Manchester, Sackville Street, Manchester, M13 9PL, UK. (e-mail: Daniel.Abara@manchester.ac.uk, Somasundar.Kannan@manchester.ac.uk, Alexander.Lanzon@manchester.ac.uk).*
[**] *Department of Electrical and Electronic Engineering, Cross River University of Technology, Cross River, Nigeria. (e-mail: Daniel.Abara@crutech.edu.ng)*

Abstract: In this paper, a low-cost single-tilting tricopter aerial vehicle is developed with optical flow estimation for indoor navigation. A dynamic model is derived and experimental data is used to obtain the actuator constants. A CAD model is then developed and is used to obtain the moments of inertia with respect to the three main axes. A control allocation algorithm is also proposed to solve the problem of the number of control inputs being more than the number of actuators since the single rotor tilt tricopter has only four actuators (3 rotors and 1 servo). A cascaded-PID control scheme is then used to stabilize the tricopter in hover mode. The simulation results yield realistic control inputs and the outputs have acceptable performance. The feasibility of the proposed scheme is then validated with some experiments on the developed tricopter platform in hover.

Keywords: Mechatronics, trirotor, tricopter, attitude control, dynamics, optical flow, indoor flight, three-rotor aircraft, hovering flight.

1. INTRODUCTION

Unmanned Aerial Vehicles (UAVs) are important for military and civil applications such as surveillance, search and rescue, detection and photography to name a few (Valavanis, 2007). This has led to increased interest in UAV research. One class of UAVs which has seen growing attention is the Vertical take-off and landing (VTOL) aircraft also termed multicopters. The VTOL configuration has attracted a lot of researchers (Valavanis, 2007) because this type of aircraft does not require a runway for take-off. The quadcopter (Lanzon et al., 2014), hexacopter (Crowther et al., 2011) and tricopter are some examples of VTOL vehicles, named after the number of rotors. For a detailed review of multicopters, see Nascimento and Saska (2019). The tricopter UAV is one which has three rotors. Escareño et al. (2008) notes that tricopters are more flexible, less-expensive and offer greater manoeuvrability compared to quadcopters. They may also yield longer flight times due to one less rotor and hence larger disc areas compared to quadcopters (Huang et al., 2009). These features have attracted a number of researchers into the study and control of tricopters: Huang et al. (2009) proposed a method where yaw is controlled by a pair of flaps mounted on the slipstream of the propellers but the complexity of this setup makes it less intuitive. Salazar-Cruz et al. (2009) proposed a T-shaped 3-rotor aircraft modelled from Newton-Euler methods and a nonlinear control based on nested saturations is used to prove stability. A novel concept was proposed in Kara Mohamed and Lanzon (2012) where all rotors can independently tilt with the aim of achieving six degrees of freedom, and H_∞ and feedback linearisation control were used to control the vehicle. A different T-shaped tricopter design which combines the features of VTOL and fixed-wing aircrafts was studied in the work of Duc Anh Ta et al. (2014). During take-off, all three rotors point upwards to achieve altitude thrust and for forward motion, the two front rotors tilt forward making the copter a fixed-wing aircaft. A similar model is proposed in Bautista et al. (2017) and Jatsun et al. (2017) where fuzzy logic control is implemented in the latter. An MPC-based controller is used to stabilize the position of a tricopter in the work by Prach and Kayacan (2018) where a control allocation algorithm is also proposed. Nonlinear Model predictive control for a tricopter is proposed by Mehndiratta and Kayacan (2018) and online learning capabilities are investigated via simulations. Instead of using conventional PIDs, Tran et al. (2019) make use of an adaptive fuzzy gain scheduling method to tune PIDs for a single tilt tricopter. While there has been some attention on the tricopter UAV, there is still insufficient experimental research to validate the tricopter concept onto real physical hardware. Most of the above works have

⋆ This work was supported by the Nigerian Petroleum Technology Development Fund (PTDF) and by the Engineering and Physical Sciences Research Council (EPSRC) [grant number EP/R008876/1]. All research data supporting this publication are directly available within this publication.

predominantly focused on theoretical and simulation results with little or no consideration of practicability. Also, only few of the models used in literature are based on real experimental data collected from physical hardware, the rest are arbitrarily chosen parameters used as numerical examples. These issues open up opportunities for further research and this is the motivation for our work.

In this paper, (1) we develop a single-tilting tricopter using low-cost materials and open-source software with optical flow included for GPS-denied environments; (2) we derive the dynamic model of the tricopter, develop an experiment to obtain the actuator constants from the acquired data and also develop a CAD model from the measured parameters of the tricopter which is used for estimating the moments of inertia; (3) we propose a control allocation scheme which allocates the actuator signals via a non-square mixer matrix due to a higher number of forces and drag torques acting on the tricopter than actuators; (4) we show the feasibility and applicability of the methods used herein by implementing cascaded-PID control to stabilize the tricopter UAV and validate the feasiblity of this work with some trial experiments on the developed platform. Furthermore, this work serves as a basis for more complex control and real-time hardware experiments with varied scenarios on the developed tricopter which is the end goal of this project.

Throughout this paper, $\mathbb{R}$ denotes the set of all real numbers, $\mathbb{R}^n$ denotes the n-dimensional $\mathbb{R}$ space, $\mathbf{I}_n \in \mathbb{R}^{n\times n}$ denotes the identity matrix of dimension n, $\text{diag}\{a, b, c\}$ represents a diagonal matrix with diagonal entries a, b, c, c_ϕ and s_ϕ denote $\cos\phi$ and $\sin\phi$ respectively, $\mathbf{a}^e$ and $\mathbf{a}^b$ denote a variable $\mathbf{a}$ given relative to the earth (inertial) and body frames respectively, and $R_e^b(\cdot)$ denotes a rotation matrix R which transforms vectors from the inertial frame to the body frame. Also, the inertial position vector and Euler angle vector are denoted as $\boldsymbol{\xi}^e$ and $\boldsymbol{\eta}$ respectively, and the body frame translational velocity and angular velocity are denoted as $\boldsymbol{\nu}^b$ and $\boldsymbol{\omega}^b$ respectively.

2. MATHEMATICAL MODELING

2.1 Coordinate rotations and systems

As shown in Fig. 1, (X_e, Y_e, Z_e) denotes the earth coordinate system which is assumed to be inertial and (X_B, Y_B, Z_B) denotes the body coordinate system with its origin fixed to the center of mass $\mathbf{G}$ of the vehicle. The transformation from the inertial frame to the body frame following the (z, y, x) sequence (Stevens et al., 2015) is encoded in the rotation matrix

$$R_e^b(\boldsymbol{\eta}) = \begin{bmatrix} c_\theta c_\psi & c_\theta s_\psi & -s_\theta \\ s_\phi s_\theta c_\psi - c_\phi s_\psi & s_\phi s_\theta s_\psi + c_\phi c_\psi & s_\phi c_\theta \\ c_\phi s_\theta c_\psi + s_\phi s_\psi & c_\phi s_\theta s_\psi - s_\phi c_\psi & c_\phi c_\theta \end{bmatrix}. \quad (1)$$

The reverse transformation from body frame to inertial frame is obtained as the inverse $R_e^b(\boldsymbol{\eta})^{-1} = R_e^b(\boldsymbol{\eta})^{\mathrm{T}} = R_b^e(\boldsymbol{\eta})$ from rotation matrix properties (Stevens et al., 2015). Similarly, the function which transforms the Euler angle velocities from the body frame to inertial frame is given in Stevens et al. (2015) as

$$\boldsymbol{\Gamma} = \begin{bmatrix} 1 & \sin\phi\tan\theta & \cos\phi\tan\theta \\ 0 & \cos\phi & -\sin\phi \\ 0 & \sin\phi\sec\theta & \cos\phi\sec\theta \end{bmatrix} \quad (2)$$

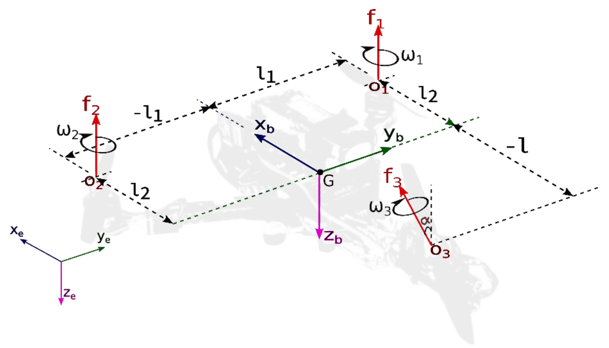

Fig. 1. Forces and torques acting on tricopter and Coordinate systems.

where θ is restricted to $(-\frac{\pi}{2}, \frac{\pi}{2})$.

2.2 Forces and Torques

The forces and drag torques produced by each rotor as depicted in Fig. 1 are assumed to be proportional to the square of the angular speeds ω_i (Prouty, 1995) since the propeller is directly coupled with the DC motor such that

$$f_i = k_t\omega_i^2 \text{ and } \tau_i = k_d\omega_i^2 \quad \forall i \in \{1, 2, 3\} \quad (3)$$

where f_i and τ_i denote the forces and drag torques respectively, k_t is the thrust constant and k_d is the drag-torque constant. The force produced by the ith rotor from Fig. 1 is

$$\mathbf{f}_i = \begin{bmatrix} 0 \\ 0 \\ -k_t\omega_i^2 \end{bmatrix} \text{ for } i \in \{1, 2\} \text{ and } \mathbf{f}_3 = \begin{bmatrix} 0 \\ -k_t\omega_3^2\sin\alpha \\ -k_t\omega_3^2\cos\alpha \end{bmatrix}$$

so that the total force from all three rotors is given as

$$\mathbf{F}_m^b = \begin{bmatrix} F_x \\ F_y \\ F_z \end{bmatrix} = \begin{bmatrix} 0 \\ -k_t\omega_3^2\sin\alpha \\ -k_t(\omega_1^2 + \omega_2^2 + \omega_3^2\cos\alpha) \end{bmatrix}. \quad (4)$$

Let (o_1, o_2, o_3) be the application points of the forces (f_1, f_2, f_3) respectively. Then the torque generated by the rotors with respect to the center of mass $\mathbf{G}$ can be expressed in the body frame as

$$\boldsymbol{\tau}_m^b = (\mathbf{G}_{o1} \times \mathbf{f}_1) + (\mathbf{G}_{o2} \times \mathbf{f}_2) + (\mathbf{G}_{o3} \times \mathbf{f}_3) \quad (5)$$

where $\mathbf{G}_{oi} = [G_{oix}\ G_{oiy}\ G_{oiz}]^{\mathrm{T}}$ is the vector of the distance of the ith rotor from the center of gravity $\mathbf{G}$ with $\mathbf{G}_{o1} = [l_2,\ l_1,\ 0]^{\mathrm{T}}, \mathbf{G}_{o2} = [l_2,\ -l_1,\ 0]^{\mathrm{T}}, \mathbf{G}_{o3} = [-l,\ 0,\ 0]^{\mathrm{T}}$, and l is the length of each rotor arm measured from each of the rotor heads to the center of mass $\mathbf{G}$, $l_1 = l\sin\frac{\pi}{3}$ and $l_2 = l\cos\frac{\pi}{3}$. Applying these in (5), the torque produced by the rotors is

$$\boldsymbol{\tau}_m^b = \begin{bmatrix} \tau_x \\ \tau_y \\ \tau_z \end{bmatrix}_m = \begin{bmatrix} l_1k_t(\omega_2^2 - \omega_1^2) \\ l_2k_t(\omega_1^2 + \omega_2^2) - lk_t\omega_3^2\cos\alpha \\ lk_t\omega_3^2\sin\alpha \end{bmatrix}. \quad (6)$$

The drag torque on the propellers is opposite to the direction of rotation of the propellers. From Fig. 1, the reaction torques of the ith rotor are given as $[0\ \ 0\ \ -\tau_i]^{\mathrm{T}}$ for $i \in \{1, 2\}$ and $[0\ \ -\tau_3\sin\alpha\ \ -\tau_3\cos\alpha]^{\mathrm{T}}$ for rotor 3 so that

$$\boldsymbol{\tau}_d^b = \begin{bmatrix} \tau_x \\ \tau_y \\ \tau_z \end{bmatrix}_d = \begin{bmatrix} 0 \\ -k_d\omega_3^2\sin\alpha \\ -k_d(\omega_1^2 + \omega_2^2 + \omega_3^2\cos\alpha) \end{bmatrix}. \quad (7)$$

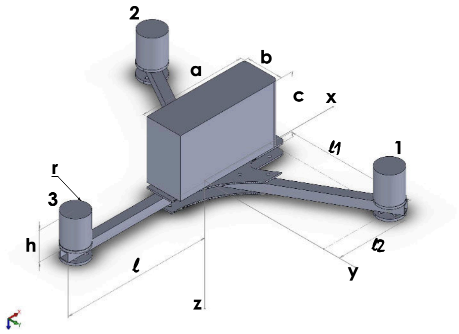

Fig. 2. Derivation of moments of inertia of a tricopter.

By summing (6) and (7) and grouping the result with (4), the expression for the total forces and torques which describes the mixer of the tricopter is obtained as

$$\begin{bmatrix} F_x \\ F_y \\ F_z \\ \tau_x \\ \tau_y \\ \tau_z \end{bmatrix} = \begin{bmatrix} 0 \\ -k_t\omega_3^2 \sin\alpha \\ -k_t(\omega_1^2 + \omega_2^2 + \omega_3^2\cos\alpha) \\ l_1 k_t(\omega_2^2 - \omega_1^2) \\ l_2 k_t(\omega_1^2 + \omega_2^2) - l k_t \omega_3^2 \cos\alpha - k_d\omega_3^2 \sin\alpha \\ l k_t\omega_3^2 \sin\alpha - k_d(\omega_1^2 + \omega_2^2 + \omega_3^2\cos\alpha) \end{bmatrix}. \quad (8)$$

2.3 Newton-Euler Model

The tricopter UAV is considered to be a rigid-body with mass m, and the total force acting on the UAV $\mathbf{F}_t^b$ is the sum of the force produced by the rotors $\mathbf{F}_m^b$ and the force due to gravity $\mathbf{F}_g^e = [0 \;\; 0 \;\; mg]^{\mathrm{T}}$, where g is the acceleration due to gravity. By using Newton-Euler methods (Stevens et al., 2015), the translational dynamics of the single-tilt tricopter is,

$$\ddot{\boldsymbol{\xi}}^e = \frac{1}{m}\left[R_e^b(\boldsymbol{\eta})^T \mathbf{F}_m^b + \mathbf{F}_g^e\right], \quad (9)$$

and the rotational dynamics is given by,

$$\dot{\boldsymbol{\eta}} = \boldsymbol{\Gamma}\boldsymbol{\omega}^b. \quad (10)$$

The angular accelerations are given as,

$$\dot{\boldsymbol{\omega}}^b = \mathbf{J}^{-1}\left[\left(-\boldsymbol{\omega}^b \times \mathbf{J}\boldsymbol{\omega}^b\right) + \boldsymbol{\tau}_t^b\right] \quad (11)$$

where $\boldsymbol{\tau}_t^b = \boldsymbol{\tau}_m^b + \boldsymbol{\tau}_d^b$ is the torque applied to the tricopter and $\mathbf{J}$ is the inertia matrix. Equations (9)–(11) together with (8) describe the nonlinear model of the tricopter. The interested reader is also referred to Kara Mohamed and Lanzon (2012) which describes a model where all three rotors can tilt.

3. MODEL PARAMETERS

3.1 Moments of Inertia

A CAD model was developed in Solidworks as depicted in Fig. 2 using the manually measured parameters of the tricopter and this was used to obtain the moments of inertia. It is assumed that the fuselage is a cuboid with length a, breadth b, height c and mass m_0, and that the motors are cylindrical with diameter D, height h and mass m_1. Note that $l_1 = \frac{\sqrt{3}}{2}l$ and $l_2 = \frac{1}{2}l$. The components J_{xy}, J_{xz} and J_{yz} are small compared to the others and are assumed negligible so that the inertia matrix becomes $\mathbf{J} = \mathrm{diag}\{J_{xx}, J_{yy}, J_{zz}\}$.

3.2 Thrust and Torque Constants

The thrust (and torque) at different speeds were measured through an experiment which consists of a thrust stand and dynamometer fitted to a wooden board mounted on a bench as in Fig. 3. The stand has a load cell for measuring the thrust, and two adjacent load cells for measuring torque. The motor is mounted between these load cells and the torque is measured using a pivot system by computing the moment between these two load cells. The thrust constant k_t and drag-torque constant k_d are

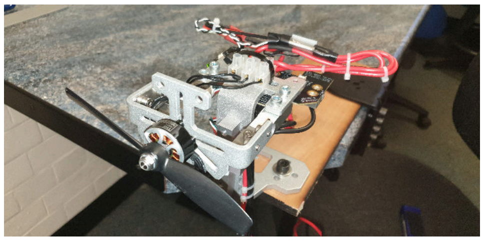

Fig. 3. Measurement of thrust and torque constants.

obtained by plotting thrust and drag torque against the square of the speed respectively so that the constants k_t and k_d are simple gradients of the best fitting line through all the data points, constructed via least squares. The experimental data used to obtain the constants k_t and k_d are shown in Fig. 4 from which we obtain $k_t = 1.591 \times 10^{-6}$kg-m and $k_d = 2.354 \times 10^{-8}$kg-m^2 when using Emax2207-eco motors with 6045 propellers on 3S (11.1V).

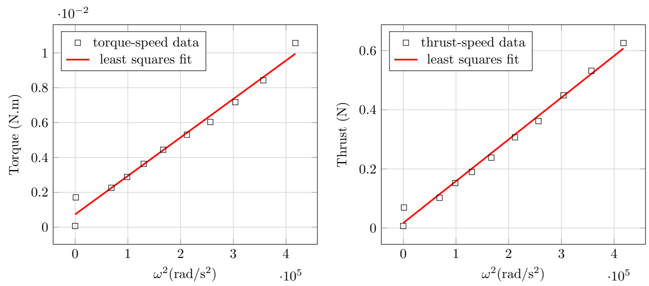

Fig. 4. Thrust and drag-torque constants data with regression fit.

All the parameters for the system including the moments of inertia, are given in Table 1.

4. HOVER CONTROL DESIGN

4.1 Linearised Model

Since we are only interested in operating the tricopter close to hover, we can simplify the nonlinear model of subsection 2.3 via linearisation. Thus, only the dynamics that describe the tricopter's behaviour when close to hovering state are considered. This leads to the assumption that $\phi \approx 0, \theta \approx 0, \psi \approx 0$ so that $\cos\phi \approx \cos\theta \approx \cos\psi \approx 1$ and $\sin\phi \approx \phi, \sin\theta \approx \theta, \sin\psi \approx \psi$. Let the state vectors be defined as $\mathbf{x} = (x, y, z, u, v, w, \phi, \theta, \psi, p, q, r)$. By applying the small angle assumptions in (9) and (10), and linearising about the operating point $\bar{\mathbf{x}} = (\bar{x}, \bar{y}, \bar{z}, 0, 0, 0, 0, 0, 0, 0, 0, 0)$, we obtain the linearised dynamics (Dydek et al., 2013),

$$\begin{cases} \ddot{\phi} = \frac{1}{J_{xx}}\tau_x, \;\; \ddot{\theta} = \frac{1}{J_{yy}}\tau_y, \;\; \ddot{\psi} = \frac{1}{J_{zz}}\tau_z, \\ \ddot{x} = -g\theta, \;\; \ddot{y} = g\phi + \frac{F_y}{m}, \;\; \ddot{z} = \frac{F_z}{m}. \end{cases} \quad (12)$$

Table 1. Summary of estimated parameters

Parameter	Estimate
arm length, l	1.625×10^{-1} m
distance of M1 from **G** on y-axis, l_1	1.4073×10^{-1} m
distance of M1/M2 from **G** on x-axis, l_2	8.125×10^{-2} m
length of fuselage, a	9.221×10^{-2} m
width of fuselage, b	4.968×10^{-2} m
height of fuselage, c	8.493×10^{-2} m
mass of motor, m_1	4×10^{-2} kg
mass of fuselage, m_0	5.83×10^{-1} kg
radius of motor, r	1.375×10^{-2} m
height of motor, h	3.276×10^{-2} m
thrust constant, k_t	1.591×10^{-6} kg-m
drag torque constant, k_d	2.354×10^{-8} kg-m^2
moment of inertia in x-axis, J_{xx}	2.33×10^{-3} kg-m^2
moment of inertia in y-axis, J_{yy}	2.71×10^{-3} kg-m^2
moment of inertia in z-axis, J_{zz}	4.36×10^{-3} kg-m^2
moment of inertia in xy-axes, J_{xy}	1.12×10^{-7} kg-m^2
moment of inertia in xz-axes, J_{xz}	-1.0×10^{-5} kg-m^2
moment of inertia in yz-axes, J_{yz}	1.44×10^{-8} kg-m^2

4.2 Control Allocation

It is not straightforward to use the vector (8) for control directly due to its complexity, and also because the mixer matrix obtained is non-square due to more control inputs $[F_y, F_z, \tau_x, \tau_y, \tau_z]^T$ than actuator signals $[\omega_1^2, \omega_2^2, \omega_3^2, \alpha]^T$. Hence, the actuator signals cannot be computed using an inverse. To solve this problem, we split the vector (8) into two groups and separate F_y noting that F_y is due to the tilting angle and the main lift force is provided by F_z. The input vector then becomes $[u_z, u_\phi, u_\theta, u_\psi]^T = [F_z, \tau_x, \tau_y, \tau_z]^T$. The term $k_d\omega_3^2 \sin\alpha$ in τ_y of (8) is assumed negligible as α is small around hover so that the main control allocation is given as the mixer

$$\begin{bmatrix} u_z \\ u_\phi \\ u_\theta \\ u_\psi \end{bmatrix} = \begin{bmatrix} -k_t & -k_t & -k_t & 0 \\ -l_1 k_t & l_1 k_t & 0 & 0 \\ l_2 k_t & l_2 k_t & -l k_t & 0 \\ -k_d & -k_d & -k_d & l k_t \end{bmatrix} \begin{bmatrix} \omega_1^2 \\ \omega_2^2 \\ \omega_3^2 \cos\alpha \\ \omega_3^2 \sin\alpha \end{bmatrix} = \mathcal{M}\boldsymbol{\Omega}. \quad (13)$$

By taking the inverse of $\mathcal{M}$, vector $\boldsymbol{\Omega}$ is given by

$$\begin{bmatrix} \Omega_1 \\ \Omega_2 \\ \Omega_3 \\ \Omega_4 \end{bmatrix} = \begin{bmatrix} -\frac{l}{2k_t(l+l_2)} u_z - \frac{1}{2l_1 k_t} u_\phi + \frac{l}{2k_t(l+l_2)} u_\theta \\ -\frac{l}{2k_t(l+l_2)} u_z + \frac{1}{2l_1 k_t} u_\phi + \frac{l}{2k_t(l+l_2)} u_\theta \\ -\frac{l_2}{k_t(l+l_2)} u_z - \frac{1}{k_t(l+l_2)} u_\theta \\ -\frac{k_d}{k_t^2 l} u_z + \frac{1}{k_t} u_\psi \end{bmatrix}. \quad (14)$$

Hence, $\omega_1 = \sqrt{\Omega_1}$, $\omega_2 = \sqrt{\Omega_2}$, $\omega_3 = \sqrt[4]{\Omega_3^2 + \Omega_4^2}$ and $\alpha = \text{atan}(\frac{\Omega_4}{\Omega_3})$. Next, $u_y = F_y$ is allocated based on the computed speed ω_3 and tilt angle α, as $u_y = -k_t\omega_3^2 \sin\alpha$, in the second allocation.

4.3 PID Cascade scheme

A PID control scheme was implemented as depicted in Fig.5. As an example, the output of the PID controller for the roll rate loop is given as

$$u_\phi = k_P(p_d - p) + k_I \int_0^t (p_d - p) - k_D p \quad (15)$$

where k_P, k_I, k_D are the gains of the PID controller, p_d is the desired roll rate, p is the measured roll rate and $(p_d - p)$ is the error. The derivative gain was applied to the output rather than the error to avoid *derivative kick*. Independent controllers similar to (15) were tuned for the angular rates, the attitude, the linear velocities and the positions respectively using Simulink. The final PID gains after some fine-tuning are summarized in Tables 2 to 4.

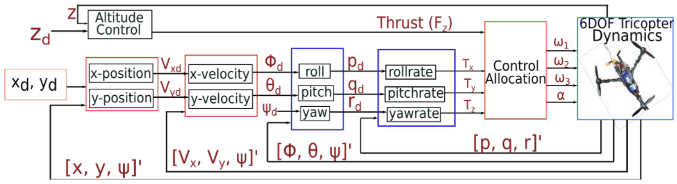

Fig. 5. Cascaded-PID control architecture.

Table 2. PID gains for attitude rate loop

	$(p, p_d) \to u_\phi$	$(q, q_d) \to u_\theta$	$(r, r_d) \to u_\psi$
k_P	0.019	0.025	0.093
k_I	0.018	0	0.139
k_D	0	0	0

Table 3. PID gains for attitude loop

	$(\phi, \phi_d) \to p_d$	$(\theta, \theta_d) \to q_d$	$(\psi, \psi_d) \to r_d$
k_P	4.75	4.75	4.75
k_I	3.85	3.83	3.85
k_D	0.74	0.74	0.74

Table 4. PID gains for velocity loop

	$(V_x, V_{xd}) \to \phi_d$	$(V_y, V_{yd}) \to \theta_d$
k_P	1.67	4.39
k_I	0	0.52
k_D	4.25	0

Table 5. PID gains for position loop

	$(x, x_d) \to V_{xd}$	$(y, y_d) \to V_{yd}$	$(z, z_d) \to u_z$
k_P	1.652	1.260	4.59
k_I	0	0	1.23
k_D	0	0	4.25

5. SIMULATION RESULTS

A simulation model was built in Matlab/Simulink using the full nonlinear dynamics of the tricopter following the scheme in Fig. 5. The maximum speed of the Emax2207-eco 1700KV motors with 6045 propellers on 3S (11.1volts) was obtained from experimental data as $\omega_{max} \approx 1639$rad/s. In order to ensure that the control inputs are feasible with respect to the physical constraints of the motor, the following control limits were set: $u_z \in (-2k_t\omega_{max}^2,\ 0)$, $u_\phi \in (-l_1 k_t\omega_{max}^2,\ l_1 k_t \omega_{max}^2)$, $u_\theta \in (-l k_t \omega_{max}^2,\ 2l_2 k_t \omega_{max}^2)$ and $u_\psi \in (-2k_d\omega_{max}^2,\ l k_t \omega_{max}^2)$. The simulation was run for 40s with the tricopter commanded to move 0.25m in the x direction and hover at a height of 0.45m. The results show that the designed controller completely stabilized the tricopter. From Fig. 6, the tricopter settles at the desired position in the x-direction after about 5 seconds and reaches the desired altitude in about 10 seconds. Fig. 7 shows that the attitude is stabilized within 6 seconds. The initial oscillatory behaviour may be due to the nonlinearities in the plant since the control is based on a linear model, but these oscillations settle within a short period of 3 seconds. The control torques (τ_x, τ_y, τ_z) are small within a range of -0.05 to 0.05kg.m^2/s^2 as observed from Fig. 8 and so the controller is practicable. The rotor speeds $(\omega_1, \omega_2, \omega_3)$ are also within the physical limits of the selected motor. It is worth noting that the speed of rotor 3 is higher than

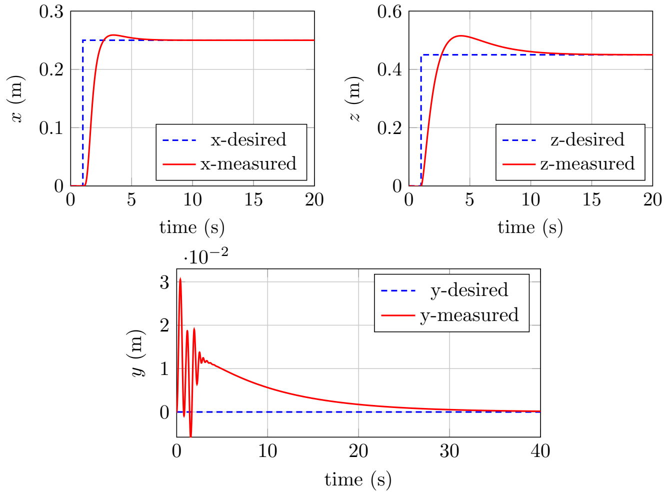

Fig. 6. x, y and z (altitude) position of tricopter in inertial coordinate frame.

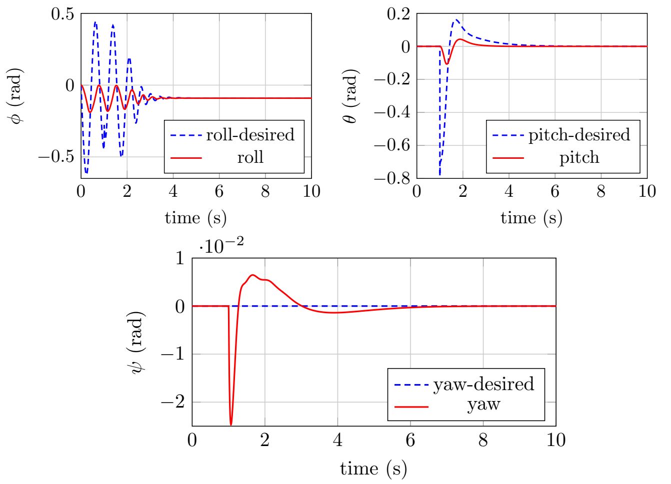

Fig. 7. Attitude of tricopter.

that of rotors 1 and 2 which are close in value. This higher speed of rotor 3 compared to rotors 1 and 2 is because, to stabilize the yaw attitude, $\alpha \approx 0.27$rad (non-zero) in steady hover as observed from Fig. 8. It then follows from Fig. 1 that, $k_t\omega_1^2 \approx k_t\omega_2^2 \approx k_t\omega_3^2 \cos\alpha \approx 2.4$N in steady hover and for this to be valid, rotor 3 has to spin faster than rotors 1 and 2. It can also be noted that the thrust at hover given as $\tau_{hover} = -mg = -7.2422$kg.m$/s^2$ is also evident from Fig. 8 which further proves the feasibility of the proposed methods.

6. EXPERIMENTAL RESULTS

6.1 Platform Description

The hardware setup of the proposed single-tilt tricopter UAV is depicted in Fig. 9 and was developed at the Control, Dynamics and Robotics laboratory at the University of Manchester. It weighs 0.739kg, has a triangular structure with three identical arms of length l, with a fixed pitch propeller driven by a Brushless DC motor mounted at the end of each arm. The tilting mechanism of the tail rotor which controls the Yaw motion is a servo-motor to which the propeller-motor assembly is attached. The servo-motor

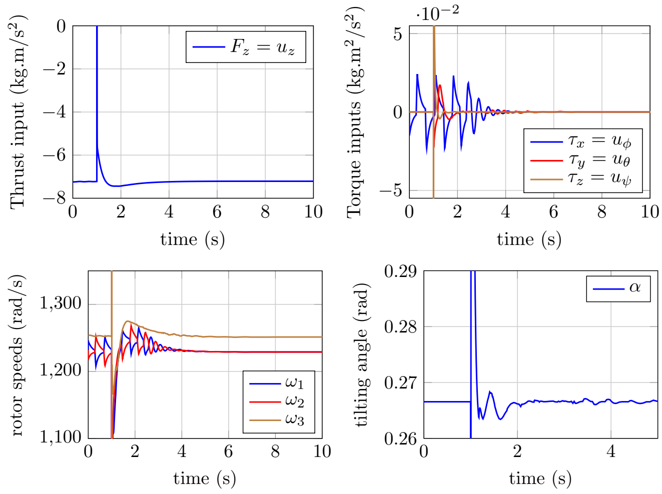

Fig. 8. Control inputs and rotor speeds of the tricopter.

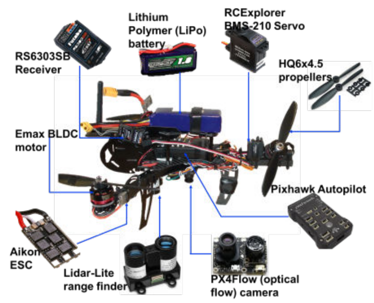

Fig. 9. Side view of the single-tilt tricopter assembly.

tilts the propeller-motor assembly through $\alpha \in (-\frac{\pi}{2}, \frac{\pi}{2})$ to generate a lateral component of the generated thrust, thereby generating a yaw torque. The *Pixhawk* autopilot (Meier et al., 2011) is used as the flight controller. It runs a 32bit processor, has 256KB RAM and 2MB Flash, with 14PWM/servo outputs, on-board sensors and several ports for connecting additional peripherals. A Lidar-Lite range-finder with PX4Flow camera is included for position estimation in order to perform indoor tests without GPS. The firmware used here is the PX4 flight stack (Honegger et al., 2013) which runs the guidance and control algorithms and QGroundControl software (Hentati et al., 2018) is used for setup and calibration.

6.2 Hover flight test

From trial tests performed, the proposed method is able to stabilize the tricopter's attitude around hover as shown in Fig. 10 although there are some peaks in roll and pitch. But this may be due to uncertainties in the plant which have not been considered by the linear model and noisy measurements from the optical flow sensor. Moreover, the PID loops were tuned independently not considering the interactions and coupling which exist between the loops of the UAV, being that it is a multi-variable system. Also, even though the PWM commands (signals sent to the individual rotors) show some oscillatory behaviour, they are not very noisy and are within configured values of 1000 to 2000. This implies a low probability of saturations occurring which is important for good performance.

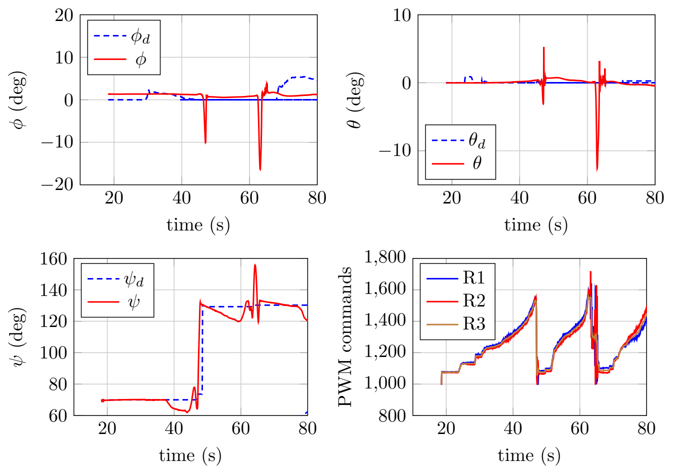

Fig. 10. Attitude and PWM commands from test.

7. CONCLUSION

In this paper, we have developed a novel tricopter UAV with a single tilt rotor. We have presented the mathematical model and proposed intuitive methods to obtain the model parameters. A control allocation scheme for obtaining motor speeds by inversion of a mixer matrix has also been proposed. These were then used to show how the loops can be closed independently and sequentially using simple PIDs. The proposed methodology aids with an intuitive design which can be tuned easily on practical hardware. The proposed control scheme has been implemented on a simulation model using parameters obtained from the tricopter platform, and some trials have been done on the developed platform for hover control. Although some areas can be improved, the test results are acceptable and provide good grounds for further research into this problem.

REFERENCES

Bautista, J.A., Osorio, A., and Lozano, R. (2017). Modeling and analysis of a tricopter/flying-wing convertible uav with tilt-rotors. In *2017 International Conference on Unmanned Aircraft Systems (ICUAS)*, pp. 672–681. June, Miami FL, USA.

Crowther, B., Lanzon, A., Maya-Gonzalez, M., and Langkamp, D. (2011). Kinematic analysis and control design for a non planar multirotor vehicle. *AIAA Journal of Guidance, Control and Dynamics*, 34(4), 1157–1171.

Duc Anh Ta, Fantoni, I., and Lozano, R. (2014). Modeling and control of a tilt tri-rotor airplane. In *proceedings of American Control Conference*, pp. 131–136. June, Montreal, Canada.

Dydek, Z., Annaswamy, A., and Lavretsky, E. (2013). Adaptive control of quadrotor uavs: A design trade study with flight evaluations. *IEEE Transactions on Control Systems Technology*, 21(4), 1400–1406.

Escareño, J., Sanchez, A., Garcia, O., and Lozano, R. (2008). Triple tilting rotor mini-UAV: Modeling and embedded control of the attitude. In *Proceedings of the American Control Conference*, pp. 3476–3481. June, Seattle, USA.

Hentati, A.I., Krichen, L., Fourati, M., and Fourati, L.C. (2018). Simulation Tools, Environments and Frameworks for UAV Systems Performance Analysis. In *proceedings of the 14th International Wireless Communications and Mobile Computing Conference*, pp. 1495–1500. June, Limassol, Cyprus.

Honegger, D., Meier, L., Tanskanen, P., and Pollefeys, M. (2013). An open source and open hardware embedded metric optical flow CMOS camera for indoor and outdoor applications. In *proceedings of the IEEE International Conference on Robotics and Automation*, pp. 1736–1741. May, Karlsruhe, Germany.

Huang, R., Liu, Y., and Zhu, J.J. (2009). Guidance, Navigation, and Control System Design for Tripropeller Vertical-Take-Off-and-Landing Unmanned Air Vehicle. *Journal of Aircraft*, 46(6), pp. 1837–1856.

Jatsun, S., Emelyanova, O., Martinez Leon, A.S., and Stykanyova, S. (2017). Control fligth of a uav type tricopter with fuzzy logic controller. In *2017 Dynamics of Systems, Mechanisms and Machines (Dynamics)*, pp. 1–5. November, Omsk, Russia.

Kara Mohamed, M. and Lanzon, A. (2012). Design and control of novel tri-rotor UAV. In *Proceedings of UKACC International Conference on Control*, pp. 304–309. September, Cardiff, UK.

Lanzon, A., Freddi, A., and Longhi, S. (2014). Flight control of a quadrotor vehicle subsequent to a rotor failure. *AIAA Journal of Guidance, Control and Dynamics*, 37(2), 580–591.

Mehndiratta, M. and Kayacan, E. (2018). Online learning-based receding horizon control of tilt-rotor tricopter: A cascade implementation. In *2018 Annual American Control Conference (ACC)*, pp. 6378–6383. June, Milwaukee WI, USA.

Meier, L., Tanskanen, P., Fraundorfer, F., and Pollefeys, M. (2011). The Pixhawk Open-Source Computer Vision Framework for Mavs. *ISPRS - International Archives of the Photogrammetry, Remote Sensing and Spatial Information Sciences*, 38(1), pp. 13–18.

Nascimento, T.P. and Saska, M. (2019). Position and attitude control of multi-rotor aerial vechcles: A survey. *Annual Reviews in Control*, 48, 129–146.

Prach, A. and Kayacan, E. (2018). An MPC-based position controller for a tilt-rotor tricopter VTOL UAV. *Optimal control applications and methods*, 39(1), 343–356.

Prouty, R.W. (1995). *Helicopter Performance, Stability and Control.* Krieger Publishing Company, Malabar, Florida.

Salazar-Cruz, S., Lozano, R., and Escareño, J. (2009). Stabilization and nonlinear control for a novel trirotor mini-aircraft. *Control Engineering Practice*, 17(8), pp. 886–894.

Stevens, B., Lewis, F., and Johnson, E. (2015). *Aircraft Control and Simulation: Dynamics, Controls Design, and Autonomous Systems.* John Wiley and Sons, Hoboken, New Jersey.

Tran, H.K., Chiou, J., Nam, N.T., and Tuyen, V. (2019). Adaptive fuzzy control method for a single tilt tricopter. *IEEE Access*, 7, 161741–161747.

Valavanis, K.P. (2007). *Advances in Unmanned Aerial Vehicles: State of the Art and the Road to Autonomy.* Springer Publishing, Dordrecht, Netherlands.